SUPPLEMENTARY INFORMATION

Data processing

A network of 5 continuously recording GPS stations (LAGU, CHIN, ENAP, GUAD and JUAN) was installed after the earthquake (Figure 1, main text). The data considered in this study covers the time period between day 20 and day 408 following the mainshock. Due to technical and logistical problems, some stations have ceased to operate for a few weeks (Figure 1). Time series of daily position were obtained using the GAMIT 10.34 software [1] aligned to the ITRF2005 [2] using 22 sites from the IGS global tracking network. In order to model the slip occurring along the subduction interface, the time series were expressed with respect to the South American plate by accounting for the secular rigid motion of the South America plate, estimated from a subset of 5 sites located in Brazil and Argentina (rms = 1.1 mm/yr). The uncertainty on each daily position is about 2.5 mm on the horizontal components and 5 mm on the vertical component (at the 67% confidence level). Figure 1 in the Supplements shows the GPS time series together with the displacements predicted from our preferred model.

Inversion Procedure

The data were inverted for slip on the fault using the PCAIM technique of Kositsky and Avouac [3]. First, a data matrix $\mathbf{X}$ is built. The element $\mathbf{X}_{ij}$ represents the displacement at station i at the j^{th} measurement at time t_j. Suppose that the network is composed of N GPS stations, each of them

recording M measurements, then the dimension of $\mathbf{X}$ is $(3N) \times M$, where the factor 3 accounts for the three components of displacement (East, North and vertical).

A classical inversion scheme solves for the slip distribution $\mathbf{L}$ such that

$$\mathbf{X} = \mathbf{G} \cdot \mathbf{L}. \tag{1}$$

Here $\mathbf{G}$ is a $(3N) \times 2n_{patch}$ matrix named the Green functions matrix and $\mathbf{G}_{ij}$ represents the displacement induced at station i due to a unit slip on patch i of the fault, divided into a total of n_{patch} sub- patches (the size $2n_{patch}$ of the Green functions matrix is due to the fact that two components of slip, e.g., along strike and up-dip, are considered since out of plane displacement is not allowed). The size of the $\mathbf{L}$ matrix is $2n_{patch} \times M$.

For the purpose of the processing the data matrix is first centered, $\bar{\mathbf{X}} = \mathbf{X} - \langle \mathbf{X} \rangle$ where $\langle \mathbf{X} \rangle_{ij} = \frac{1}{M} \sum_{k=1}^{M} \mathbf{X}_{ik}$. Doing so, each time series in $\mathbf{X}$ has a zero mean. Next, we proceed with a Singular Value Decomposition (SVD) $\bar{\mathbf{X}}$,

$$\bar{\mathbf{X}} = \mathbf{U} \cdot \mathbf{S} \cdot \mathbf{V^t}, \tag{2}$$

where $(...)^t$ means matrix transpose. The matrices $\mathbf{U}$, $\mathbf{S}$ and $\mathbf{V}$ are of respective size $3N \times 3N$, $3N \times M$ and $M \times M$. The matrix $\mathbf{S}$ is diagonal with r ($< \min(3N, M)$) non zero eigenvalues λ_i, $i = 1, r$, r being the rank of $\mathbf{S}$. The eigenvalues are conventionally ordered decreasingly. Note that the fraction of the variance of the data matrix accounted by the eigenvalue $k = 1, r$ is simply $\frac{\lambda_k^2}{\sum_{i=1}^{r} \lambda_i^2}$. This decomposition can therefore be an efficient way to filter the data [4].

Eq. (1) and (2) may be combined to infer the slip history $\mathbf{L}$ on the fault

$$\mathbf{L} = \mathbf{L}_0 + (\mathbf{G}^{-1}\mathbf{U}) \cdot \mathbf{S} \cdot \mathbf{V}^{\mathbf{t}}, \tag{3}$$

where $\mathbf{L}_0 = \mathbf{G}^{-1} \cdot \langle \mathbf{X} \rangle$ represents the slip on the fault that accounts for the mean displacement of each station. Looking at (3), it can be seen that the inversion is now performed considering the $\mathbf{U}$ matrix, a $(3N) \times (3N)$ matrix, instead of the matrix $\mathbf{X}$ in the classical inversion scheme. $\mathbf{X}$ being a $(3N) \times M$ matrix, the difference in terms of computational time can be quite significant for a large number of measurements M.

Using Eq. (3), it can be easily shown that

$$\mathbf{\Delta L}_{ij} = \sum_{k=1}^{r} \lambda_k \mathbf{P}_{ik} \mathbf{V}_{jk}, \tag{4}$$

where $\mathbf{\Delta L} = \mathbf{L} - \mathbf{L}_0$. It follows from Eq. (4) that the slip on patch i at time t_j is obtained by summing the contribution $\lambda_k \mathbf{P}_{ik} \mathbf{V}_{jk}$ of each separate eigenvalue λ_k. Note that the vector $\mathbf{P} = \mathbf{G}^{-1} \cdot \mathbf{U}$ is only space dependent (matrix of size $2n_{patch} \times 3N$) while $\mathbf{V}$ is only time dependent (square matrix of size M). Consequently, the spatial evolution of slip is contained in the $\mathbf{P}$ vector, while the time evolution is accounted for by the $\mathbf{V}$ vector. The decomposition given in (4) is called a Principal Component Analysis (PCA).

This decomposition requires measurements at all stations at all epochs. Several techniques can be used in case of missing data [3]. Here the missing data were interpolated using a functional of the form $c_1 \log(1 + c_2(\exp(t/t_r) - 1)))$ derived assuming frictional afterslip [5], c_1, c_2 and t_r being parameters to be adjusted. The interpolated data were penalized in the inversion by assigning

them an uncertainty equal to the maximal uncertainty measured at the station and displacement component considered. The interpolated points are not considered in the estimation of the chi-square fit between the observed displacements and those predicted from the afterslip models.

Figure 2 of the Supplements shows the contribution of each component to the GPS times series analyzed in this study. The first three components account for about 97.1% of the original signal (respectively 92.7, 2.7 and 1.7% for the first, second and third components). Considering that the contribution of higher order components is negligible and within the measurement noise, we use only the first three components to perform the inversion. Eq. (4) simplifies then to

$$\mathbf{\Delta L}_{ij} \approx \lambda_1 \mathbf{P}_{i1} \mathbf{V}_{j1} + \lambda_2 \mathbf{P}_{i2} \mathbf{V}_{j2} + \lambda_3 \mathbf{P}_{i3} \mathbf{V}_{j3}. \quad (5)$$

The temporal evolution of slip is given by the eigenvectors $\mathbf{V}_1 = \mathbf{V}_{j1}$, $\mathbf{V}_2 = \mathbf{V}_{j2}$ and $\mathbf{V}_3 = \mathbf{V}_{j3}$, $j = 1, M$, displayed on Figure 3. The eigenvector $\mathbf{V}_1$ evolves as the logarithm of time, as commonly observed for postseismic slip. The temporal evolution of the second and third eigenvectors $\mathbf{V}_2$ and $\mathbf{V}_3$ is less systematic, and quite noisy. The red continuous curves were obtained using a Gaussian filter of width $M/20$. The filtered series are used in the inversion.

As commonly done (see for instance Miyazaki et al. (2004) [6]), Eq. (3) is solved with some regularization constraints. We constrain the slip distribution to be smooth by minimizing the Laplacian of the slip distribution. Because of its linearity, this operator can be applied directly on the eigenvectors $\mathbf{U}$. A parameter γ is introduced to weight the constraint put on smoothing, and $\mathbf{L}$

is then determined from the least-squares solution of

$$\begin{pmatrix} \mathbf{C}\cdot\mathbf{G} \\ \frac{1}{\gamma^2}\boldsymbol{\Delta} \end{pmatrix} \cdot \mathbf{L} = \begin{pmatrix} \mathbf{C}\cdot\mathbf{U} \\ 0 \end{pmatrix}. \quad (6)$$

In (6), $\mathbf{C}$ is a $3N \times 3N$ diagonal matrix built taking the inverse of the diagonal matrix which elements are the mean errors in the GPS measurements. Doing so, a weight depending on the quality of the GPS measurements at each station is applied. The matrix $\boldsymbol{\Delta}$ corresponds to the discrete Laplacian operator, modified in order to tapper slip on the down-dip and sides of the fault model. No such tapering is imposed along the up-dip edge of the fault. Decreasing the smoothing parameter γ increases the effect of the smoothing. A reasonable range of $\gamma = 0.002 - 0.02$ was found to give the best compromise between smoothing and goodness of the fit. Finally, the slip on the fault $\mathbf{L}$ is determined by inverting Eq. (6) under a positivity constraint, forcing the slip vectors on each patch to point towards the trench.

Modeling of interseismic coupling

To assess the pattern of interseismic coupling along the megathrust offshore Central Peru we have used interseismic geodetic measurements augmented with sea bottom geodetic measurements [7,8]. The modeling approach and strategy is identical to that of Chlieh et al. (2008) [9]. The GPS data are inverted for slip on the megathrust based on the backslip model [10], and Green functions computed using elastic dislocation theory [11]. Following Bevis et al. (2001) [12], we take into account shortening across the sub-Andean zone and considered three plates (Nazca, the forearc and Andean Plateau, stable South America). We also assume that the Euler vectors describing the Nazca and

forearc motion relative to stable South America are coaxial. We solved for the best fitting model of interseismic coupling with proper account for the trade-off between coupling along the megathrust and shortening across the sub-Andes. The best-fitting model yields a shortening rate of 5 mm/yr across the sub-Andes, identical to the value estimated by Bevis et al (2001) [12]. The megathrust strikes 321° E and dips 18° to the east. The geodetic data used to put constraints on interseismic coupling on the megathrust in our study area are listed in Table 1 of the Supplements. The rake is free to vary between 220° and 260°. Table 2 in the Supplements lists the average interseismic coupling coefficient for various models obtained by constraining the moment rate deficit to a fixed value. The average coupling is computed on the portion of the megathrust that intersects the trench between 11° and 16° of latitude south (Figure 3 of the main text) and at depth between 0 and 40 km. We selected that depth range for consistency with the depth range generally considered to evaluate seismic coupling [13]. We find that the models with an average coupling between 0.41 and 0.62 provides an equivalent fit to these data but that the misfit to the measurements increases beyond that range.

Lon.	Lat.	East Disp.	North Disp.	Error East	Error North	NAME	Reference
-73.93	-13.99	13.2	2	2.4	1.5	CANA	K2001
-72.78	-15.14	13.9	4.2	2.9	0.9	COTA	K2001
-71.98	-13.51	7.1	6.1	1.3	0.9	CUSO	K2001
-75.21	-12.13	11.4	3.2	1.5	1	HUAN	K2001
-70.4	-14.08	4.3	1.2	1.3	1.1	MACU	K2001
-71.41	-12.91	1	5.7	1.6	1.1	PPAT	K2001
-76.36	-13.87	26.7	1.6	1.2	0.8	PRAC	K2001
-72.56	-12.65	4.3	4.8	4.4	1.7	QLLO	K2001
-76.44	-12.95	25.7	2.8	2.1	1.2	QUIL	K2001
-77.02	-12.04	18.3	0.6	4.4	2.3	SCRI	K2001
-74.45	-15.75	24.2	-1	3.1	2.2	TANA	K2001
-75.62	-14.66	21.8	1.4	3.5	2.3	ZAMA	K2001
-77.612	-11.238	29.4	-1.51	1.425	0.875	SALI	G2005
-78.165	-12.168	46.57	0.82	1.875	1.125	Land	G2005
-78.486	-12.272	43.26	11.43	1.975	2.1	Seaw	G2005

Table 1: Horizontal GPS velocities in the South America reference frame using the pole of rotation defined by Kendrick et al. [2003] [14]. References for the data are K2001 for Kendrick et al. (2001) and G2005 for Gagnon et al. (2005) [7,8].

Model Name	Moment Rate Deficit (N.m/yr)	Average Coupling	χ_r^2
Mo1	$0.68\,10^{19}$	0.20	4.6
Mo2	$1.04\,10^{19}$	0.30	2.1
Mo3	$1.43\,10^{19}$	0.41	1.7
Mo4	$1.63\,10^{19}$	0.48	1.7
Mo5	$1.76\,10^{19}$	0.53	1.7
Mo6	$1.98\,10^{19}$	0.62	1.7
Mo7	$2.25\,10^{19}$	0.73	2.0
Mo8	$2.44\,10^{19}$	0.79	3.6

Table 2: Variation of the moment rate deficit for GPS data including 5 mm/yr of back-arc shortening. The equivalent moment rate deficit and average coupling is computed between latitudes -16 and -11 and depth less than 40 km. The corresponding reduced chi-square (χ_r^2) are listed in column 4.

Estimating the contribution of aseismic slip to long term fault slip

Let us call C_{inter} the contribution of aseismic slip in the interseismic period, C_{cos} the contribution of coseismic slip, C_{post} the contribution of afterslip, and C_{trans} the contribution of slip transients (such as slow slip events). During an entire cycle, the sum of all contributions should be equal to one

$$C_{inter} + C_{cos} + C_{post} + C_{trans} = 1. \tag{7}$$

The total contribution C_{as}^{tot} of aseismic slip during the cycle is given by

$$C_{as}^{tot} = C_{inter} + C_{post} \approx 1 - C_{cos}, \tag{8}$$

after use of Eq. (7) and neglecting the contribution of transient slip events (which is unknown but should be negligible compare to inter-, co- and postseismic slip).

In the section 'Modeling of interseismic coupling' of the Supplements, we have found that interseismic coupling $\chi = 1 - C_{inter} = 0.41 - 0.62$. Similarly, we have found in section 'Uncertainty on postseismic moments' that $C_{post}/C_{cos} = \alpha$, with $\alpha = 0.08 - 0.27$ between days 20 and 408 after the mainshock, and $\alpha = 0.22 - 0.41$ when extrapolated to the time of the mainshock. Introducing α and χ into Eq. (8) leads to

$$C_{cos} \approx \frac{\chi}{1+\alpha}, \tag{9}$$

$$C_{post} \approx \frac{\alpha}{1+\alpha}\chi, \tag{10}$$

and finally

$$C_{as}^{tot} \approx 1 - \frac{\chi}{1+\alpha}. \tag{11}$$

Using $\chi = 0.41 - 0.62$ and $\alpha = 0.08 - 0.27$ yields $C_{as}^{tot} \approx 0.43 - 0.68$, while $\alpha = 0.22 - 0.41$ gives $C_{as}^{tot} \approx 0.49 - 0.71$. We conclude that aseismic slip accounts for 50 to 70 % of the moment released during the earthquake cycle.

Postseismic models: sensitivity and robustness tests

In this section we present various models that allow to evaluate the sensitivity to the model parameters and identify the robust features needed to fit the data within uncertainties.

Two type of models are considered: variable and fixed rake models. In the variable rake models, Eq (6) is solved with no Additional constraints. The Green matrix has a size $(3N) \times 2n_{patch}$, the factor 2 in $2n_{patch}$ arising from the fact that the slip vector has two components (up-dip and strike-slip). The presence of the 2D discrete Laplacian smoothing operator will also impose smooth variations in the rake variations. The fixed rake model is simply obtained imposing the direction of the slip vector. In this case we again solve for Eq. (6) but consider a modified Green matrix. The $\mathbf{G}$ matrix we consider has a size $(3N) \times n_{patch}$ because it is only computed along the imposed rake direction.

Models are assessed according to a misfit function defined here as $\chi_r^2 = \frac{1}{N_{tot}} \sum_{i=1}^{N_{tot}} \frac{(U_{mod}(i) - U_{obs}(i))^2}{\sigma(i)^2}$ where N_{tot} is the total number of observations, U_{mod} and U_{obs} are respectively the modeled and observed displacement fields with error measurements σ. The interpolated data were not considered in the estimation of χ_r^2.

Figure 4B shows the cumulative slip model considering a fixed rake of $67°$ and a smoothing parameter of $\gamma = 0.002$ (smooth model). Figure 4C shows the same for a rougher model with $\gamma = 0.01$ (rough model). The black arrows show the slip vectors for cells which slip amplitude is greater than 20% of the peak slip. The pink contours correspond to the coseismic model of Sladen et al. (2009) [15]. For both the smooth and rough models, most afterslip occurs south of the model, in continuation of the Nazca ridge. In the smooth model, the peak slip is of the order of 0.3 m and is widely spread. In the rough model of Figure 4C, the peak slip is of the order of 0.8 m and is concentrated near the trench (patch A). A second significant zone of afterslip can be observed near the hypocenter (patch B). This second patch corresponds to a peak of the density of aftershocks (see Figure 2 of the main text). Both models demonstrate a good complementary between co- and postseismic slip, i.e., significant postseismic slip is located on the surrounding of the coseismic asperities. The rough model of Figure 4C shows a better agreement between peak postseismic slip and peak aftershocks density than the smooth model of Figure 4B which does not correlate with the peak of aftershocks density near the hypocenter. Not surprisingly, the rough model is in closer agreement with the data ($\chi_r^2 \approx 2.54$) than the smooth one ($\chi_r^2 \approx 4.46$).

Figure 4D shows the cumulative slip model considering a variable rake and a smoothing parameter of $\gamma = 0.002$ (smooth model). Figure 4E shows the same for a rougher model with $\gamma = 0.01$ (rough model). The variable rake model is consistent with the features of the fix rake model, although peak slips are different (respectively 0.2 and 0.4 m for the smooth and rough model), Again, the rough model is in closer agreement with the data ($\chi_r^2 \approx 2.69$) than the smooth one ($\chi_r^2 \approx 5.95$). In both the smooth and rough variable rake models, the rake is mostly perpendicular

to the trench. In the rough model, rotations of the rake are observed on the edge of the afterslip asperities, but remains limited. As expected, the fluctuations of the rake are lower in the smooth model than in the rough because high smoothing smooths rake variations.

All of the models presented in the previous section show a robust pattern which is the presence of postseismic slip along the axis of the subduction Nazca ridge (patch A). A feature observed on rougher models such as in Figure 4C and 4E is the existence of a second postseismic patch west of the hypocenter (patch B). In order to test the robustness of those features, we performed inversions forcing no slip on patches A or B, while keeping the rest of the parameters of the best fit models unchanged. The results are compiled in Table 3.

Figure 4F shows the prediction of a model similar to Figure 4C but forced to show no slip on the Nazca ridge. This constraint degrades dramatically the fit to the data, the reduced chi-square rising from 2.54 to 15.4. The same feature is observed for the variable rake model as may be seen in Figure 4H. In this case, the reduced chi-square rises from 2.69 to 17.1. In both the fixed and variable models, aftershocks density and postseismic slip are anti-correlated when no slip is forced in continuation to the Nazca ridge. Note in particular the anomalous rake (left-lateral motion) appearing near the trench in the variable rake model of Figure 4H. All those features lead to the conclusion that a model where no afterslip occurs along the Nazca ridge is not acceptable.

Figure 4G shows the prediction of a model similar to Figure 4C but forced to show no slip on patch B. The reduced chi-square is $\chi^2_r \approx 2.8$ instead of 2.54, so that the agreement with the data is rather similar. Postseismic slip is concentrated along the Nazca ridge and in the upper

part of the fault. The correlation between the peak of aftershocks density above patch B has now disappeared (by construction of this model). The slip patch previously located near the hypocenter has now moved towards the trench. The same conclusions can be reached for the variable rake model. Figure 4I shows the prediction of a model similar to Figure 4E but forced to show no slip on patch B. The reduced chi-square is $\chi_r^2 \approx 3.85$ instead of 2.69, a moderate degradation of the fit. The slip pattern near along the Nazca ridge remains unchanged. The effect of forcing slip to vanish near the hypocenter is to move former patch B towards the trench.

In the view of Figures 4F-I, postseismic slip along the Nazca ridge is a required feature to match the observations. Removing this contribution of slip decreases the fit to the data dramatically, and leads to physical inconsistencies (anti-correlation between postseismic slip and aftershocks activity). Postseismic slip on the second patch B significantly improves the fit to the data while making the model physically sound. But removing this contribution still leads to an acceptable description of the GPS observations.

Model	Rake	Smooth. param. γ	Slip on patch A	Slip on patch B	χ^2_r
A	variable	0.01	y	y	2.7
B	67 °	0.002	y	y	4.5
C	67 °	0.01	y	y	2.5
D	variable	0.002	y	y	6.0
E	variable	0.01	y	y	2.7
F	67 °	0.01	n	y	15.4
G	67 °	0.01	y	n	2.8
H	variable	0.01	n	y	17.1
I	variable	0.01	y	n	3.9

Table 3: Summary table of sensitivity tests.

Uncertainty on postseismic moments

Figure 5 of this supplement shows the chi-square χ^2_r as a function of the postseismic moment for the entire parameter space we have explored.

In this section we explore the range of admissible postseismic slip-potency (or equivalently moment, computed assuming a shear modulus of 50 GPa). We have obtained a suite of models by varying the smoothing parameter γ between 10^{-4} and 10^3 assuming either a variable rake or a fixed rake (with a rake of 67^o). We find that the misfit increases very rapidly as the moment gets smaller than about 9e19 N.m. All the models obtained have a moment smaller than 3e20 N.m. We thus estimate the range of admissible moment to $9\,10^{19} < M_0 < 3\,10^{20}$ N.m. This means that afterslip between days 20 and 408 after the mainshock released a moment estimated to between 8 and 27 % of the co-seismic moment. Those estimates can be extrapolated to the time of the mainshock assuming that postseismic relaxation is governed by frictional afterslip.

According to Perfettini et al. (2005) [16], postseismsic slip evolves as a function of time as $V_{pl}t_r \log\left(1 + \frac{V^+}{V_{pl}}(\exp\frac{t}{t_r} - 1)\right)$, where V_{pl} is the long-term (e.g., plate) velocity, V^+ the initial afterslip velocity and t_r the relaxation time. For $V_{pl} = 62$ mm/yr (a value representative of the area), the best fit to $\mathbf{V}_1$ (the temporal eigenvector relative to the first component) (see Figure) yields $t_r = 1.2$ yr and $\frac{V^+}{V_{pl}} = 92$. Since $\mathbf{V}_1$ is the dominant component, it is reasonable to assume that the seismic moment has the same temporal evolution. When extrapolated to the time of the mainshock, the postseismic moment rises to represent between 22 and 41 % of coseismic slip.

1. Herring, T., King, R. & McClusky, S. (2008).

2. Altamimi, Z., Collilieux, X., Legrand, J., Garayt, B. & Boucher, C. Itrf2005: A new release of the international terrestrial frame based on time series of station positions and earth orientation parameters. *J. Geophys. Res.* **112**, doi:10.1029/2007JB004949 (2007).

3. Kositsky, A. P. & Avouac, J.-P. Inverting geodetic time-series with a principal component analysis-based inversion method (pcaim). *J. Geophys. Res.* (2009). In press.

4. Aoki, Y. & Scholz, C. Vertical deformation of the japanese islands, 1996-1999. *J. Geophys. Res.* **108**, doi:10.1029/2002JB002129 (2003).

5. Perfettini, H. & Avouac, J.-P. Postseismic relaxation driven by brittle creep: A possible mechanism to reconcile geodetic measurements and the decay rate of aftershocks, application to the chi-chi earthquake, taiwan. *J. Geophys. Res.* **109**, doi:10.1029/2003JB002488 (2004).

6. Miyazaki, S., Segall, P., Fukuda, J. & Kato, T. Space time distribution afterslip following the 2003 tokachi-oki earthquake: Implications for variations in fault zone frictional properties. *Geophys. Res. Lett.* **31**, doi:10.1029/2003GL019410 (2004).

7. Kendrick, E., Bevis, M., Jr., R. S. & Brooks, B. An integrated crustal velocity field for the central andes. *Geochem. Geophys. Geosyst.* **2**, doi:10.1029/2001GC000191 (2001).

8. Gagnon, K., Chadwell, C. D. & Norabuena, E. Measuring the onset of locking in the peru-chile trench with gps and acoustic measurements. *Nature* **434**, 205–208 (2005).

9. Chlieh, M., Avouac, J.-P., Sieh, K., Natawidjaja, D. & Galetzka, J. Heterogeneous coupling of the sumatran megathrust constrained by geodetic and paleogeodetic measurements. *J. Geophys. Res.* **113**, doi:10.1029/2007JB004981 (2008).

10. Savage, J. A dislocation model of strain accumulation and release at a subduction zone. *J. Geophys. Res.* **88**, 4984–4996 (1983).

11. Okada, Y. Internal deformation due to shear and tensile faults in a half-space. *Bull. Seismol. Soc. Am.* **82**, 1018–1040 (1992).

12. Bevis, M. *et al.* On the strength of interplate coupling and the rate of back arc convergence in the central andes: An analysis of the interseismic velocity field. *Geochem. Geophys. Geosyst.* **2**, doi:10.1029/2001GC000198 (2001).

13. Ruff, L. & Kanamori, H. Seismic coupling and uncoupling at subduction ones. *Tectonophysics* **99**, 99–117 (1983).

14. Kendrick, E. *et al.* The nazca-south america euler vector and its rate of change. *Journal of South American Earth Sciences* **16**, 125–131 (2003).

15. Sladen, A. *et al.* Source model of the 2007 $mw8.0$ pisco, peru earthquake-implications for seismogenic behavior of subduction megathrusts. *J. Geophys. Res.* (2009). In press.

16. Perfettini, H., Avouac, J.-P. & Ruegg, J. Geodetic displacements and aftershocks following the 2001, $m_w = 8.4$ peru earthquake: Implications for the mechanics of the earthquake cycle along subduction zones. *J. Geophys. Res.* **109**, doi: 10.1029/2004JB003522 (2005).

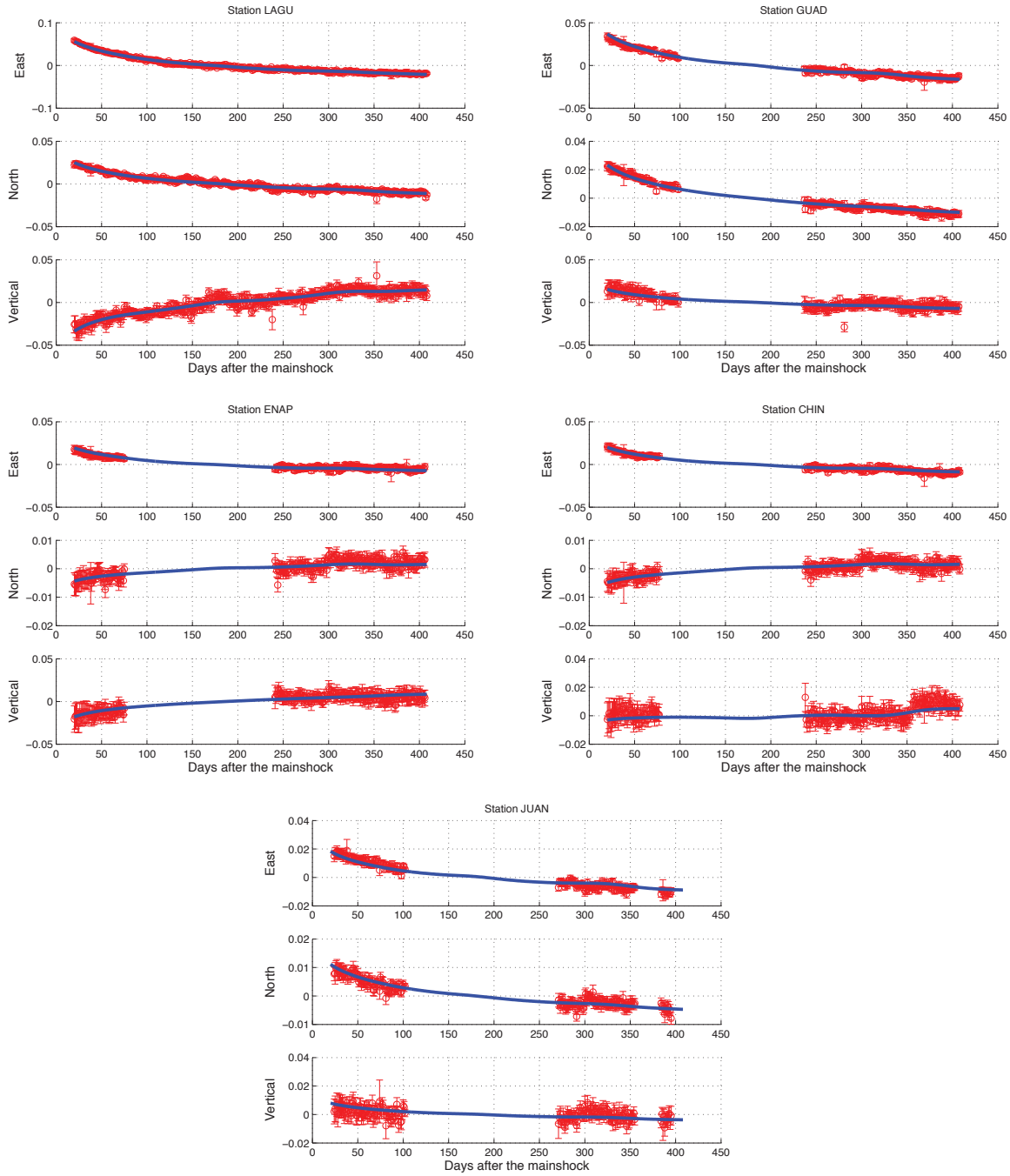

Figure 1 Time series (red open circles with corresponding error bars) at station LAGU, GUAD, ENAP, CHIN and JUAN during the days 20-408 after the mainshock. Solid blue lines show the displacements predicted from our preferred model (model A in Table 1, Figure 4A).

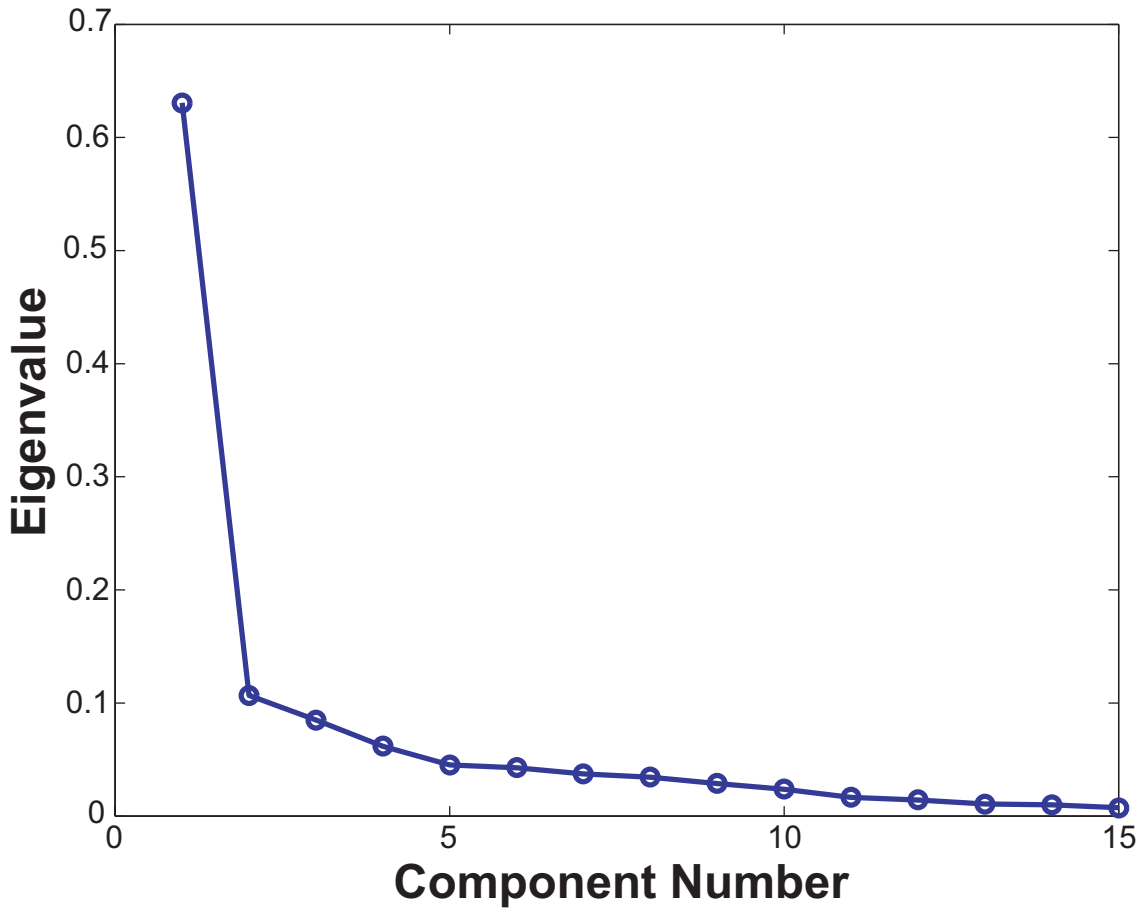

Figure 2 Eigenvalues of the PCA decomposition sorted by decreasing amplitude.

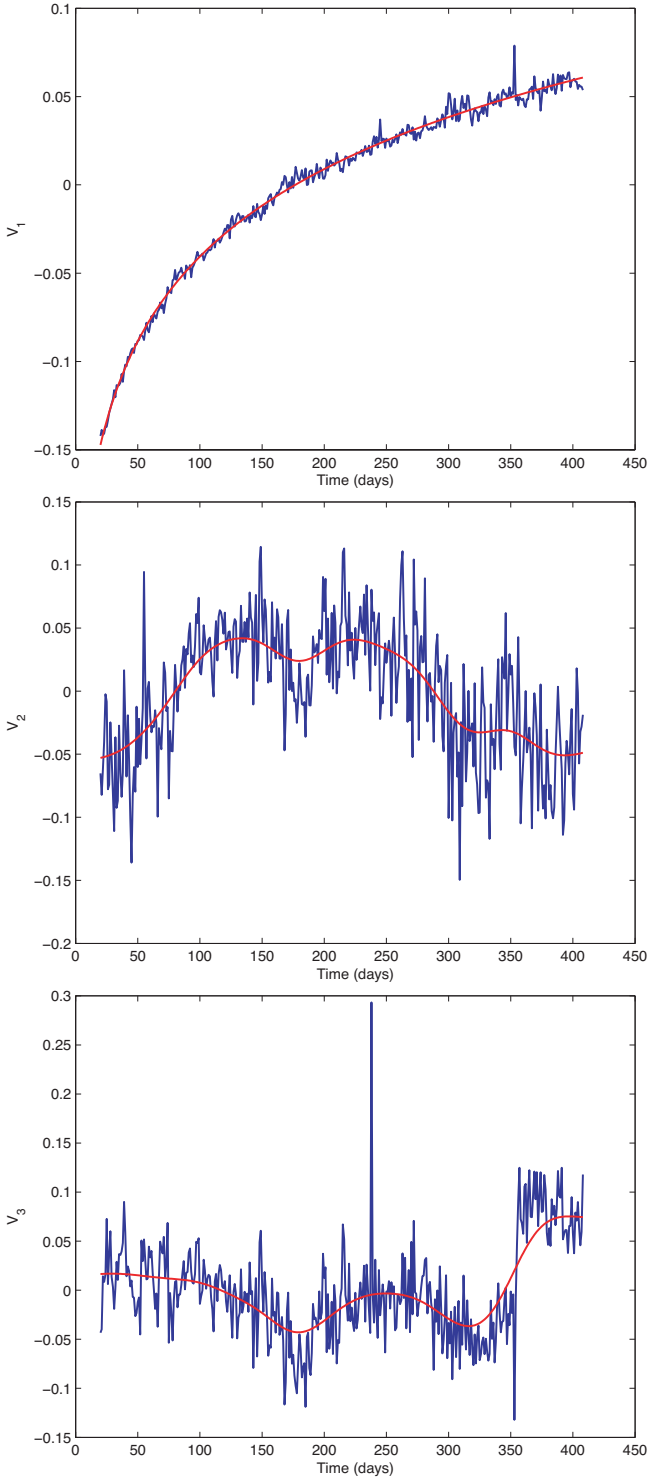

Figure 3 (from top to bottom) Temporal eigenvectors $\mathbf{V}_{j1}$, $\mathbf{V}_{j2}$ and $\mathbf{V}_{j3}$, $j = 1, M$.

Figure 4A-C

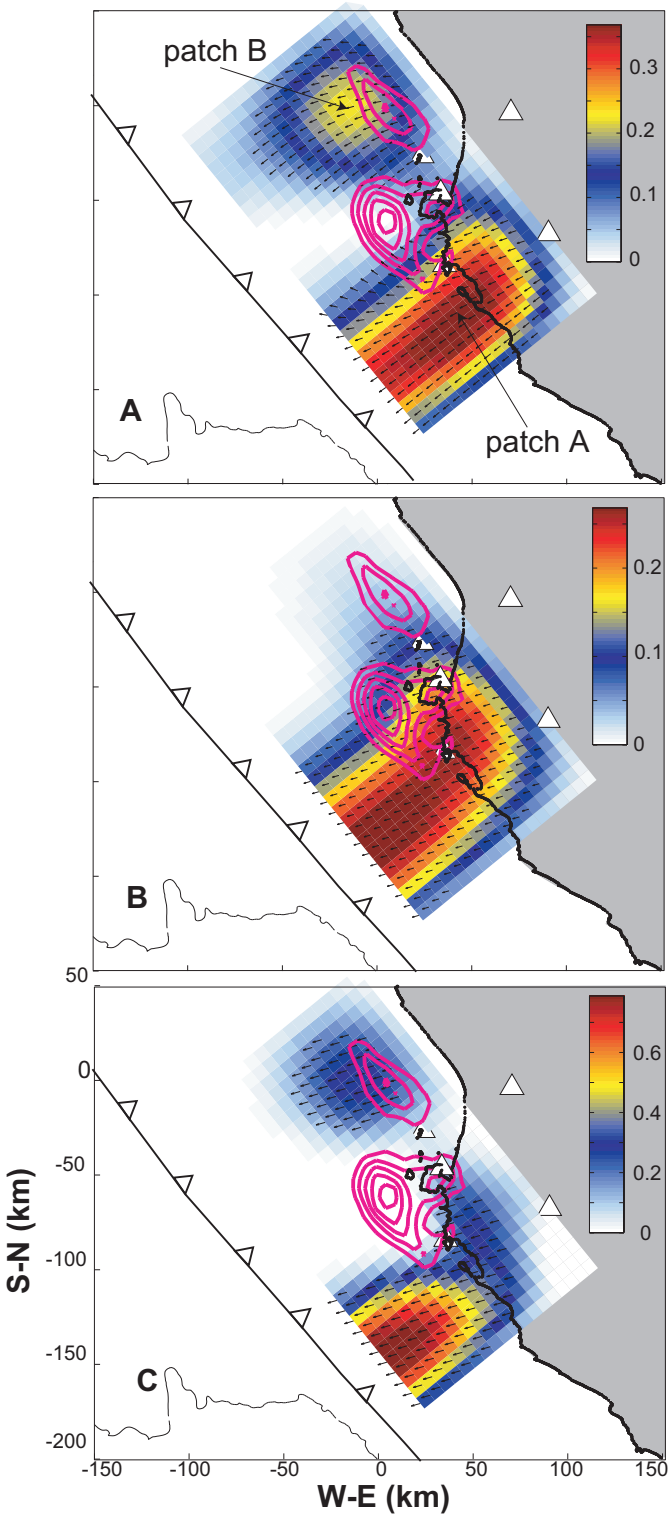
patch B
patch A
A
B
C
0.3
0.2
0.1
0
0.2
0.1
0
0.6
0.4
0.2
0
50
0
-50
-100
-150
-200
S-N (km)
-150
-100
-50
0
50
100
150
W-E (km)

Figure 4D-F

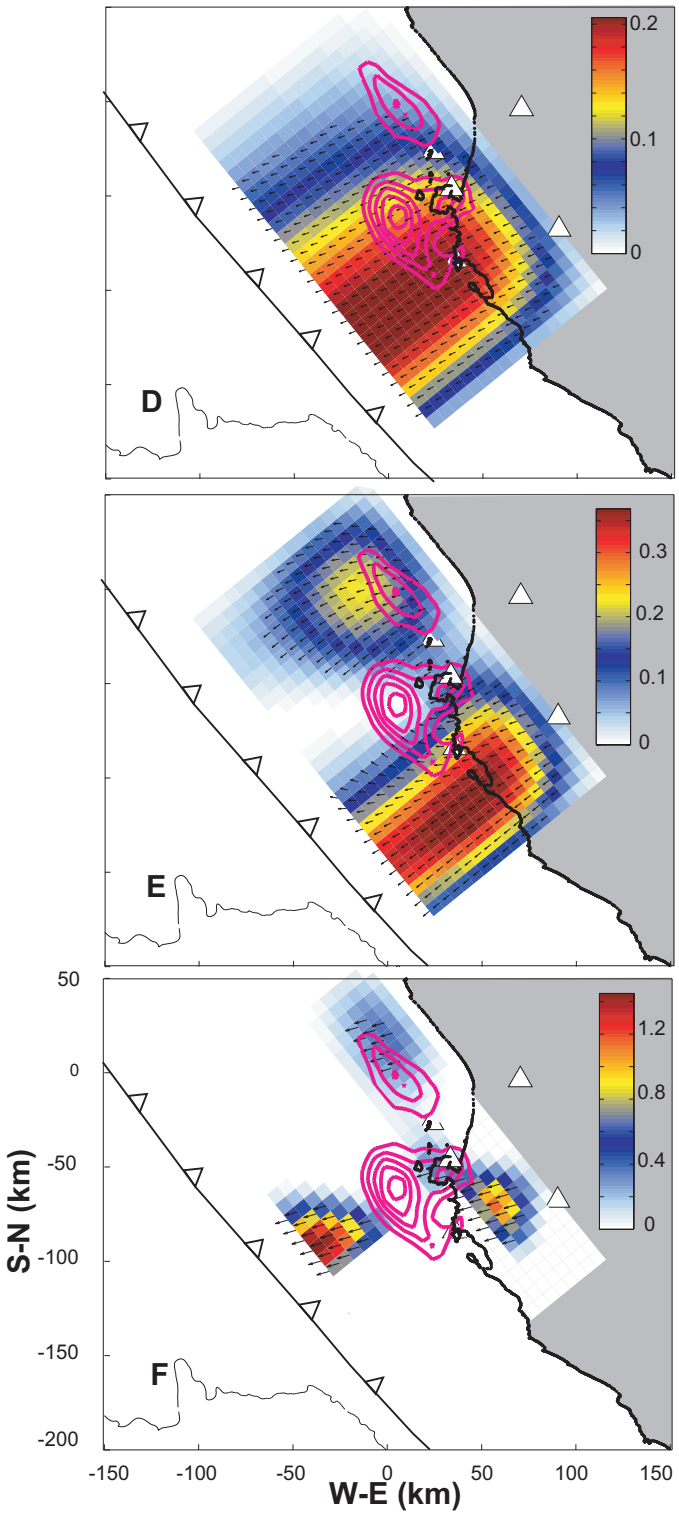
D
E
F
0.2
0.1
0
0.3
0.2
0.1
0
1.2
0.8
0.4
0
50
0
-50
-100
-150
-200
S-N (km)
-150
-100
-50
0
50
100
150
W-E (km)

Figure 4G-I

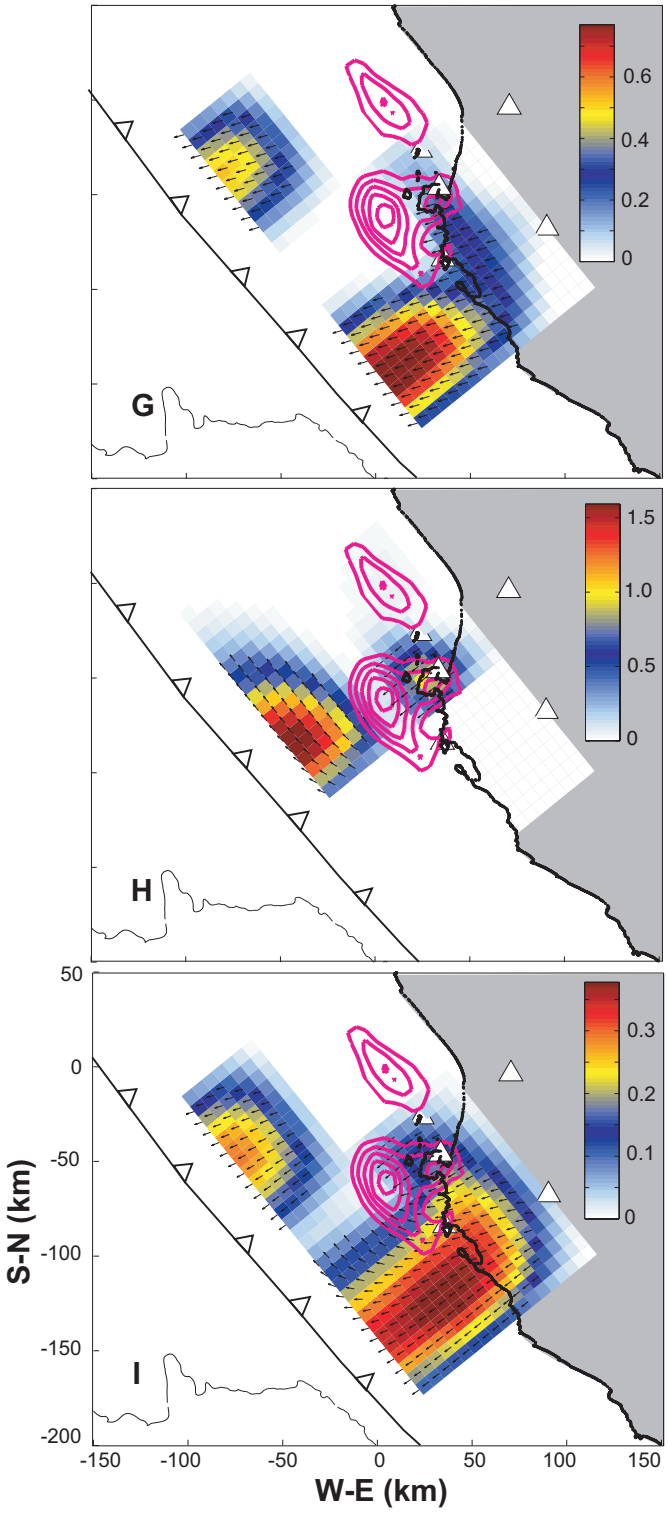

Figure 4 Slip models considered in this study. See main text for details.

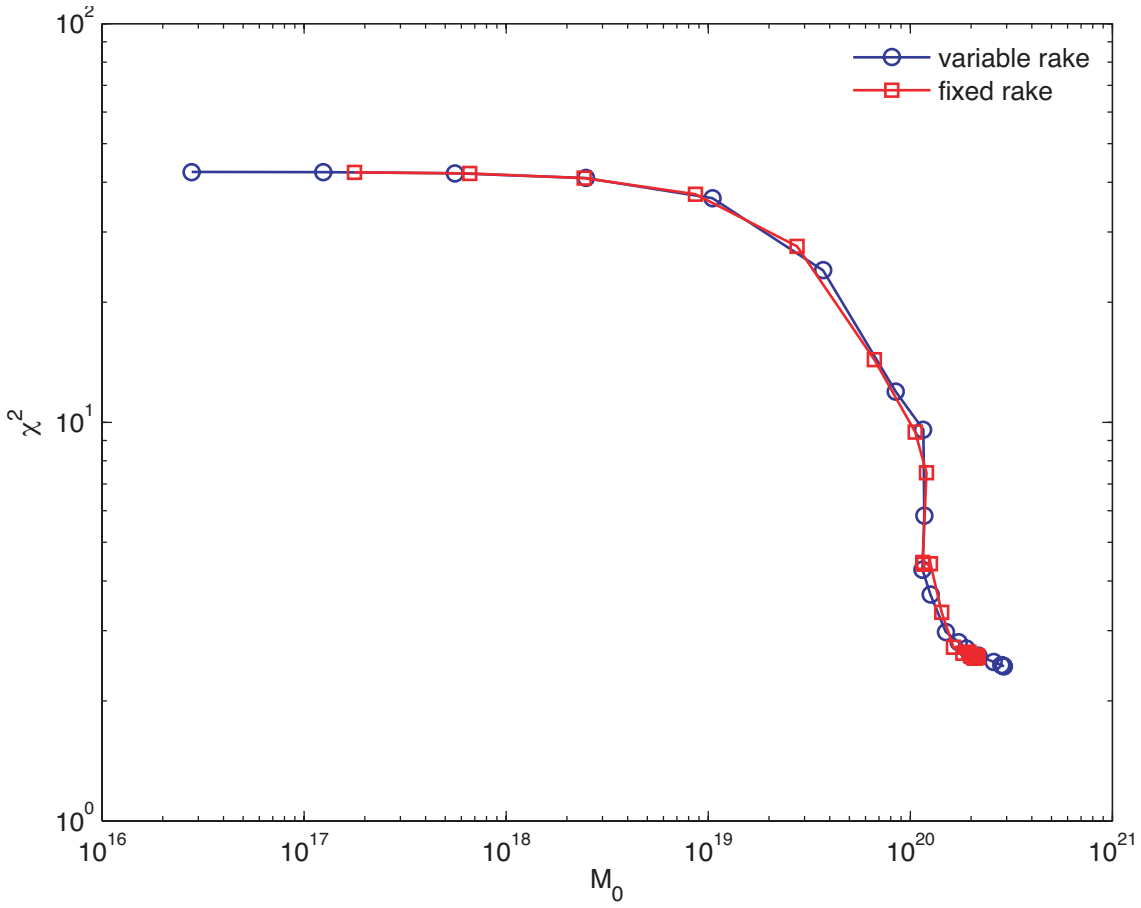

Figure 5 χ^2_r vs. postseismic moment. See main text for details.